



Article

Theoretical Analysis of a Fractional-Order LLCL Filter for Grid-Tied Inverters

Xiaogang Wang^{1,*} , Ruidong Zhuang¹ and Junhui Cai²¹ School of Mechanical and Electrical Engineering, Guangzhou University, Guangzhou 510006, China² School of Electronics and Communication Engineering, Guangzhou University, Guangzhou 510006, China

* Correspondence: wxg@gzhu.edu.cn

Abstract: The LLCL-filter-based grid-tied inverter performs better than the LCL-type grid-tied inverter due to its outstanding switching-frequency current harmonic elimination capability, but the positive resonance peak must be suppressed by passive or active damping methods. This paper proposes a class of fractional-order LLCL (FOLLCL) filters, which provides rich features by adjusting the orders of three inductors and one capacitor of the filter. Detailed analyses are performed to reveal the frequency characteristics of the FOLLCL filter; the orders must be selected reasonably to damp the positive resonance peak while reserving the negative resonance peak to attenuate the switching-frequency harmonics. Furthermore, the control system of the grid-tied inverter based on the FOLLCL filter is studied. When the positive resonance is suppressed by the intrinsic damping effect of the FOLLCL filter, the passive or active damper can be avoided; the grid current single close-loop is adequate to control the grid-tied inverter. For low-frequency applications, proportional-resonant (PR) controller is more suitable for the FOLLCL-type grid-tied inverter compared with the proportional-integral (PI) and fractional-order PI controllers due to its overall performance. Simulation results are consistent with theoretical expectations.

Keywords: LLCL filter; active damping; fractional-order; grid-tied inverter; proportional-resonant (PR) control

**Citation:** Wang, X.; Zhuang, R.; Cai, J.Theoretical Analysis of a Fractional-Order LLCL Filter for Grid-Tied Inverters. *Fractal Fract.* **2023**, *7*, 135. <https://doi.org/10.3390/fractalfract7020135>

Academic Editors: Behnam Mohammadi-Ivatloo and Arman Oshnoei

Received: 9 January 2023

Revised: 25 January 2023

Accepted: 29 January 2023

Published: 31 January 2023



Copyright: © 2023 by the authors. Licensee MDPI, Basel, Switzerland. This article is an open access article distributed under the terms and conditions of the Creative Commons Attribution (CC BY) license (<https://creativecommons.org/licenses/by/4.0/>).

1. Introduction

The grid-tied inverter is widely used in renewable energy generation; the voltage-source inverter (VSI) interfaces with the grid through a low-pass filter to limit the excessive current harmonics. A third-order LCL filter is the most popular solution over a first-order L filter due to its smaller size, lower cost, and better harmonic attenuation capability [1–5]. However, large inductance should be selected for an LCL filter in low-frequency applications to suppress the more abundant current harmonics. To solve this problem, a high-order LLCL filter has been proposed in [6] and further developed in [7–15]. Based on the LCL filter, a small inductor is inserted in series with the capacitor to form a series resonant branch. The series resonant frequency is thus designed to further attenuate the switching harmonics. The total harmonic distortion (THD) of the grid current will be much lower with LLCL-type inverters compared with LCL-type ones in low-frequency applications.

However, the LLCL filter retains the positive resonant feature of the LCL filter, which causes system instability. Passive or active dampers are used to mitigate the impact of the positive resonance, leading to power loss or control complexity. It is even worse that the capacitor current feedback, the most commonly used active damping method, may introduce a negative resistance and cause instability due to the control delay [8].

In recent years, the fractional-order modeling of power converters has been paid much attention because the inductors and capacitors, the key components of power converters, have fractional-order characteristics, or can be specially designed as fractional-order components. The research of fractional-order power converters began from the modeling of

DC–DC converters. In [16], fractional calculus and the circuit-averaging technique are used to model the buck converter. This technique is also used to build the model of the fractional-order magnetic coupled boost converter [17]. The fractional-order model of the buck converter based on the Caputo–Fabrizio derivative is presented in [18]. The Riemann–Liouville derivative is also used to obtain more accurate models of the fractional-order buck converter [19] and fractional-order buck–boost converter [20]. Instead of considering the complex definitions of fractional calculus, the harmonic balance principle and equivalent small parameter method are used to describe the fractional-order DC–DC converters [21]. Different from the above studies, time domain expressions for fractional-order DC–DC converters are derived in [22]. The modeling methods for fractional-order DC–AC converters are also reported in the literature. In [23], the Caputo derivative method is used to build the model of the voltage source converter, and small-signal analysis and averaging state-space model-based analysis are developed. The fractional-order model of the three-phase voltage source PWM rectifier is constructed in [24]; the Caputo fractional calculus operator is used to describe the fractional-order characteristics of the inductor and capacitor. In addition, the influence of the orders of the inductors and the capacitor on the operating characteristics of the PWM rectifier is studied. In [25], an LC α L filter-based grid-connected inverter is modeled and a filter design example is given. However, the above literature only focuses on the modeling methods; the control strategies are not considered.

On the other hand, fractional-control theories are developed to control the power converters. The fractional-order PID control method is employed to regulate DC–DC converters [26,27]; the results show that the method achieves less overshoot and a faster recovery time compared to the integer-order PID regulator. In [28], the fractional-order adaptive sliding mode control approach is proposed for fractional-order buck–boost converters, which shows stronger robustness under various disturbances. For LCL-type grid-tied inverters, an active damping method based on fractional-order proportional-derivative (PD) grid current feedback is presented in [29], which shows better performance compared to the integer-order PD damping method. In [30], a capacitive current fractional proportional-integral feedback strategy is proposed to increase the limit of the damping region of the LCL grid-tied inverter under the weak grid condition. A fractional-order LCL (FOLLCL) filter-based grid-tied inverter is studied in [31]; the capacitor current feedback loop can be omitted by only changing the orders of the passive components. Especially, PI and fractional-order PI controllers especially are designed for this grid-tied inverter.

Considering the advantages of fractional-order converters, this paper proposes a fractional-order LLCL-type grid-tied inverter, which can avoid the use of an active damper. The contributions of this paper include the following points:

- i. The characteristics of the FOLLCL filter is analyzed, including the condition of resonance, magnitude–frequency characteristic, phase–frequency characteristic, and the impacts of inductor and capacitor orders on the characteristics.
- ii. The control system of the FOLLCL-type grid-tied inverter is given. Active damping can be avoided, thus improving the ease of control and saving the cost of the control system.
- iii. The performances of the FOLLCL-type grid-tied inverter based on PI, PI $^\lambda$, and PR control are analyzed through four cases. Among these three control methods, the most suitable one for the FOLLCL-type grid-tied inverter without an active damper is determined.

The remainder of the paper is organized as follows: Section 2 introduces the integer-order LLCL (IOLLCL) filter and makes a comparison between the IOLLCL filter and the IOLCL filter. Section 3 analyzes the characteristics of the FOLLCL filter, including resonant frequency, magnitude–frequency characteristic, and phase–frequency characteristic. In Section 4, the structure of the control system of the FOLLCL-type grid-tied inverter is described. Based on the expression of loop gain, the system performance is analyzed. Four cases are presented to discuss the performance of the FOLLCL-type grid-tied inverter.

The simulation results are given in Section 5 to validate the theoretical analysis. Finally, Section 6 concludes this paper.

2. Integer-Order LLCL Filter

An VSI can connect the power grid through an LLCL filter to form a grid-tied inverter. The equivalent circuit of a single-phase integer-order LLCL-filter-based grid-tied inverter is shown in Figure 1, where L_1 and L_2 are the inverter-side and grid-side inductors, a small inductor L_f and a capacitor C_f composing a series resonant circuit, u_i and i_1 are the inverter output voltage and current, u_g and i_g are the grid voltage and current, and i_c is the capacitor current.

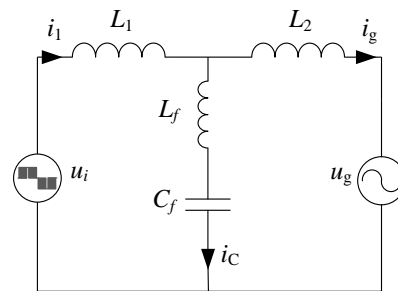


Figure 1. Equivalent circuit of a single-phase integer-order LLCL-filter-based grid-tied inverter.

The transfer function $i_g(s)/u_i(s)$ of the IOLLCL filter can be derived as

$$G_{IO} = \frac{i_g(s)}{u_i(s)} \Big|_{u_g(s)=0} = \frac{L_f C_f s^2 + 1}{(L_1 L_2 C_f + (L_1 + L_2) C_f L_f) s^3 + (L_1 + L_2) s} \quad (1)$$

Figure 2 illustrates the bode diagrams of $i_g(s)/u_i(s)$ for both the IOLLCL filter and IOLCL filter while all the other parameters are the same except for L_f . The specific parameters of the filters are given in Table 1. Unlike the IOLCL filter, the IOLLCL filter has two resonance peaks: a negative one and a positive one; the resonance frequencies are f_{rp1} (ω_{rp1}) and f_{rp2} (ω_{rp2}), respectively. When the VSI operates under the condition of the dual-carrier sine-wave PWM, the uppermost harmonics of i_g are around the switching frequency $2f_s$. Therefore, f_{rp1} is designed to be equal to $2f_s$ to attenuate such harmonics. The positive resonance peak at f_{rp2} , as in the resonance peak at f_{rp} for the IOLCL filter, would lead to system instability in grid-tied inverter applications and should be damped by passive or active methods.

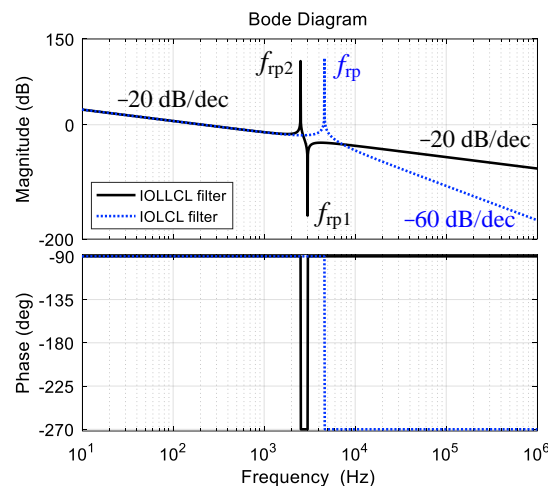


Figure 2. Frequency-response characteristic of the IOLLCL filter.

Table 1. Filter Parameters.

Parameter	Symbol	Value
inverter-side inductor	L_1	600 μH
grid-side inductor	L_2	150 μH
series resonant circuit inductor	L_f	70.362 μH
series resonant circuit capacitor	C_f	10 μF

The negative resonant frequency of the IOLLCL filter is

$$\omega_{rp1} = \sqrt{\frac{1}{L_f C_f}} \tag{2}$$

The positive resonant frequency of the IOLLCL filter is

$$\omega_{rp2} = \sqrt{\frac{L_1 + L_2}{L_1 L_2 C_f + L_f C_f (L_1 + L_2)}} \tag{3}$$

It can also be seen from Figure 2 that the IOLLCL and IOLCL filters have similar low-frequency magnitude characteristics, while the IOLCL filter exhibits a better attenuation ability at a high-frequency band than the IOLLCL filter. However, overall, compared with the IOLCL filter, the grid current can obtain lower total harmonic distortion with the IOLLCL filter.

3. Fractional-Order LLCL Filter

The IOLLCL filter in the grid-tied inverter can be replaced by an FOLLCL filter to achieve better performance. The FOLLCL filter consists of four components: three inductors and a capacitor, as shown in Figure 3. In this paper, an LLCL filter can be called a fractional-order LLCL filter, with all or part of its components being fractional-order ones.

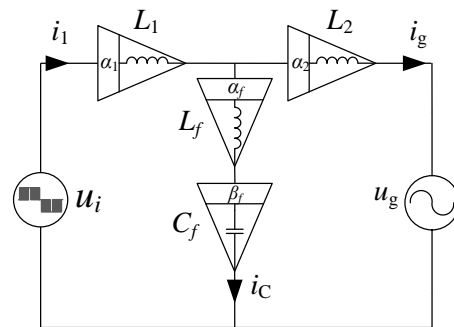


Figure 3. Equivalent circuit of a single-phase fractional-order LLCL-filter-based grid-tied inverter.

The transfer function from input (inverter output voltage u_i) to output (grid current i_g) is expressed as

$$G_{FO} = \frac{i_g(s)}{u_i(s)} = \frac{L_f C_f s^{\alpha_f + \beta_f} + 1}{L_1 L_2 C_f s^{\alpha_1 + \alpha_2 + \beta_f} + C_f L_f L_1 s^{\alpha_1 + \alpha_f + \beta_f} + C_f L_f L_2 s^{\alpha_2 + \alpha_f + \beta_f} + L_1 s^{\alpha_1} + L_2 s^{\alpha_2}} \tag{4}$$

where α_1 , α_2 , α_f , and β_f are the orders of L_1 , L_2 , L_f , and C_f , respectively. The magnitude–frequency and phase–frequency characteristic expressions obtained from (4) are quite complex. To simplify the analysis, set $\alpha_1 = \alpha_2 = \alpha$; (4) is rewritten as

$$G_{FO} = \frac{i_g(s)}{u_i(s)} = \frac{L_f C_f s^{\alpha_f + \beta_f} + 1}{L_1 L_2 C_f s^{2\alpha + \beta_f} + C_f L_f (L_1 + L_2) s^{\alpha + \alpha_f + \beta_f} + (L_1 + L_2) s^\alpha} = \frac{L_f C_f s^{\alpha_f + \beta_f} + 1}{L_1 L_2 C_f s^\alpha [s^{\alpha + \beta_f} + B s^{\alpha_f + \beta_f} + A]} \tag{5}$$

where $A = (L_1 + L_2)/(L_1L_2C_f)$ and $B = L_f(L_1 + L_2)/(L_1L_2)$. Substitute $(j\omega)^\alpha = \omega^\alpha \cos(\alpha\pi/2) + j\omega^\alpha \sin(\alpha\pi/2)$ into (5); the mathematical model in frequency domain can be obtained as

$$G_{FO}(j\omega) = \frac{L_f C_f \omega^{\alpha_f + \beta_f} \left[\cos \frac{(\alpha_f + \beta_f)\pi}{2} + j \sin \frac{(\alpha_f + \beta_f)\pi}{2} \right] + 1}{L_1 L_2 C_f \omega^\alpha \left(\cos \frac{\alpha\pi}{2} + j \sin \frac{\alpha\pi}{2} \right) \left[\omega^{\alpha + \beta_f} \cos \frac{(\alpha + \beta_f)\pi}{2} + A + j \omega^{\alpha + \beta_f} \sin \frac{(\alpha + \beta_f)\pi}{2} + B \omega^{\alpha_f + \beta_f} \cos \frac{(\alpha_f + \beta_f)\pi}{2} + j B \omega^{\alpha_f + \beta_f} \sin \frac{(\alpha_f + \beta_f)\pi}{2} \right]} \quad (6)$$

The magnitude–frequency characteristic of G_{FO} is expressed as

$$|G_{FO}(j\omega)| = \frac{1}{L_1 L_2 C_f \omega^\alpha} \frac{\sqrt{\left[L_f C_f \omega^{\alpha_f + \beta_f} \cos \frac{(\alpha_f + \beta_f)\pi}{2} + 1 \right]^2 + \left(\sin \frac{(\alpha_f + \beta_f)\pi}{2} \right)^2}}{\sqrt{\left(\omega^{\alpha + \beta_f} \cos \frac{(\alpha + \beta_f)\pi}{2} + A + B \omega^{\alpha_f + \beta_f} \cos \frac{(\alpha_f + \beta_f)\pi}{2} \right)^2 + \left(\omega^{\alpha + \beta_f} \sin \frac{(\alpha + \beta_f)\pi}{2} + B \omega^{\alpha_f + \beta_f} \sin \frac{(\alpha_f + \beta_f)\pi}{2} \right)^2}} \quad (7)$$

3.1. Resonant Frequencies

Define angular frequency ω_{r1} as follows:

$$\omega_{r1} = \left[-\frac{1}{L_f C_f \cos[(\alpha_f + \beta_f)\pi/2]} \right]^{\frac{1}{\alpha_f + \beta_f}} \quad (8)$$

Then, the numerator of (7) can be expressed as

$$\text{num}(|G_{FO}|) = \sqrt{\left[-\left(\frac{\omega}{\omega_{r1}}\right)^{\alpha_f + \beta_f} + 1 \right]^2 + \left(\sin \frac{(\alpha_f + \beta_f)\pi}{2} \right)^2} \quad (9)$$

When $\omega = \omega_{r1}$, (9) can be reduced to

$$\text{num}(|G_{FO}|) = \left| \sin \frac{(\alpha_f + \beta_f)\pi}{2} \right| \quad (10)$$

If $\alpha_f + \beta_f = 2n$ (n is an integer), $\sin[(\alpha_f + \beta_f) n\pi/2] = 0$, and $|G_{FO}(j\omega_{r1})|$ as shown in (7) is zero. It means that the magnitude–frequency characteristic of the FOLLCL filter has a negative resonance (series resonance) peak at $\omega = \omega_{r1}$. According to the present literature, the orders of the actually realizable fractional-order inductors and capacitors are greater than 0 and less than 2, so n is set to 1 in this research. Therefore, to attenuate the switching-frequency current ripple in grid-tied inverter applications, the sum of α_f and β_f must equal 2. Substitute $\alpha_f + \beta_f = 2$ back into (8); the negative resonant frequency can be obtained as

$$\omega_{rp1} = \sqrt{\frac{1}{L_f C_f}} \quad (11)$$

It can be seen from (8) that the series resonance peak of the FOLLCL filter has the same form as the IOLLCL filter when $\alpha_f + \beta_f = 2$. Series resonance is the most critical feature for the FOLLCL filter, so the following analysis is based on the relationship of $\alpha_f + \beta_f = 2$.

Substitute $\alpha_f + \beta_f = 2$ to (7); the denominator of (7) is expressed as

$$\text{den}(|G_{FO}|) = L_1 L_2 C_f \omega^\alpha \sqrt{\left(\omega^{\alpha + \beta_f} \cos \frac{(\alpha + \beta_f)\pi}{2} + A - B\omega^2 \right)^2 + \left(\omega^{\alpha + \beta_f} \sin \frac{(\alpha + \beta_f)\pi}{2} \right)^2} \quad (12)$$

Define angular frequency ω_{r2} as follows:

$$\omega_{r2} = \left[-\frac{A - B\omega^2}{\cos[(\alpha + \beta_f)\pi/2]} \right]^{\frac{1}{\alpha + \beta_f}} \quad (13)$$

Therefore, (12) can be expressed as

$$\text{den}(|G_{FO}|) = L_1 L_2 C_f \omega^\alpha \sqrt{\left[-\left(\frac{\omega}{\omega_{r2}}\right)^{\alpha+\beta_f} (A - B\omega^2) + A - B\omega^2\right]^2 + \left(\omega^{\alpha+\beta_f} \sin \frac{(\alpha+\beta_f)\pi}{2}\right)^2} \tag{14}$$

When $\omega = \omega_{r2}$, (14) can be reduced to

$$\text{den}(|G_{FO}|) = L_1 L_2 C_f \omega^\alpha \sqrt{\left(\omega_{r2}^{\alpha+\beta_f} \sin \frac{(\alpha+\beta_f)\pi}{2}\right)^2} \tag{15}$$

If $\alpha + \beta_f = 2$, $\sin[(\alpha + \beta_f)\pi/2] = 0$, and $|G_{FO}(j\omega_{r2})|$ as shown in (7) is positive infinity. It means that the magnitude–frequency characteristic of the FOLLCL filter has a positive resonance peak at $\omega = \omega_{r2}$. Substitute $\alpha + \beta_f = 2$ back into (13); the positive resonant frequency can be obtained as

$$\omega_{rp2} = \sqrt{\frac{L_1 + L_2}{L_1 L_2 C_f + L_f C_f (L_1 + L_2)}} \tag{16}$$

It can be seen from (16) that the FOLLCL filter has the same expression of positive resonance peak as the IOLLCL filter when $\alpha_f + \beta_f = 2$ and $\alpha + \beta_f = 2$.

Theorem 1. *When $\alpha_1 = \alpha_2 = \alpha$, the negative resonance (series resonance) peak of the FOLLCL filter exists only when $\alpha_f + \beta_f = 2$; the resonant frequency is $\omega_{rp1} = \sqrt{1/L_f C_f}$. The positive resonance peak of the FOLLCL filter exists only when $\alpha_f + \beta_f = 2$ as well as $\alpha + \beta_f = 2$; the resonant frequency is $\omega_{rp2} = \sqrt{(L_1 + L_2) / [L_1 L_2 C_f + L_f C_f (L_1 + L_2)]}$. The positive resonant frequency ω_{rp2} is always less than the negative resonant frequency ω_{rp1} .*

Theorem 1 essentially reveals the resonant conditions for FOLLCL filters and provides a criterion to estimate whether an FOLLCL filter has resonance peaks. Orders α , α_f , and β_f of a conventional IOLLCL filter are all equal to 1. Both conditions $\alpha_f + \beta_f = 2$ and $\alpha + \beta_f = 2$ are satisfied; therefore, the IOLLCL filter is just a special case of the FOLLCL filter. Moreover, the positive resonance peak can be avoided according to Theorem 1 by choosing reasonable orders for the inverter-side inductor L_1 , grid-side inductor L_2 , and capacitor C_f . Passive or active damping approaches used in an IOLLCL filter can be omitted for an FOLLCL filter.

3.2. Magnitude–Frequency Characteristic

As previously mentioned, $\alpha_f + \beta_f = 2$ must be satisfied for the FOLLCL filter, so (7) can be arranged as

$$|G_{FO}(j\omega)| = \frac{1}{L_1 L_2 C_f \omega^\alpha} \frac{|-L_f C_f \omega^2 + 1|}{\sqrt{\left(\omega^{\alpha+\beta_f} + (A - B\omega^2) \cos \frac{(\alpha+\beta_f)\pi}{2}\right)^2 + (A - B\omega^2)^2 \sin^2 \frac{(\alpha+\beta_f)\pi}{2}}} \tag{17}$$

(1) When $\omega \ll \omega_{rp2}$, $L_f C_f \omega^2 \ll 1$, and $A - B\omega^2 \approx A$, (17) can be further expressed as

$$|G_{FO}(j\omega)| = \frac{1}{L_1 L_2 C_f \omega^\alpha} \frac{1}{\sqrt{\left(\omega^{\alpha+\beta_f} + A \cos \frac{(\alpha+\beta_f)\pi}{2}\right)^2 + A^2 \sin^2 \frac{(\alpha+\beta_f)\pi}{2}}} \tag{18}$$

Define intermediate variables ω_{t1} and ω_{t2} as follows:

$$\omega_{t1} = \left| A \cos \frac{(\alpha + \beta_f)\pi}{2} \right|^{\frac{1}{\alpha + \beta_f}} \tag{19}$$

$$\omega_{t2} = \left| A \sin \frac{(\alpha + \beta_f)\pi}{2} \right|^{\frac{1}{\alpha + \beta_f}} \tag{20}$$

Substitute (19) and (20) into (18); the magnitude–frequency characteristic can be derived as

$$|G_{FO}(j\omega)| = \frac{1}{L_1 L_2 C_f \omega^\alpha} \frac{1}{\sqrt{(\omega^{\alpha + \beta_f} + \tau \omega_{t1}^{\alpha + \beta_f})^2 + \omega_{t2}^{2(\alpha + \beta_f)}}} \tag{21}$$

where $\tau = 1$ ($\alpha + \beta_f \in (0, 1] \cup [3, 4)$) or $\tau = -1$ ($\alpha + \beta_f \in (1, 3)$).

When $\omega \ll \omega_{t1}$, $(\omega/\omega_{t1})^{\alpha + \beta_f} \approx 0$ and $\tau^2 = 1$, (21) can be simplified as

$$\begin{aligned} |G_{FO}(j\omega)| &= \frac{1}{L_1 L_2 C_f \omega^\alpha \omega_{t1}^{\alpha + \beta_f}} \frac{1}{\sqrt{((\omega/\omega_{t1})^{\alpha + \beta_f} + \tau)^2 + (\omega_{t2}/\omega_{t1})^{2(\alpha + \beta_f)}}} \\ &\approx \frac{1}{L_1 L_2 C_f \omega^\alpha} \frac{1}{\sqrt{\omega_{t1}^{2(\alpha + \beta_f)} + \omega_{t2}^{2(\alpha + \beta_f)}}} = \frac{1}{L_1 L_2 C_f A \omega^\alpha} \end{aligned} \tag{22}$$

The log magnitude–frequency characteristic and the slope of its asymptote are expressed as (23) and (24).

$$L(\omega) \approx -20 \lg(L_1 L_2 C_f A) - 20\alpha \lg \omega \tag{23}$$

$$\frac{dL(\omega)}{d \lg \omega} \approx -20\alpha \text{ dB/dec}, \omega \ll \omega_{t1} \tag{24}$$

(2) When $\omega \gg \omega_{rp1}$, $L_f C_f \omega^2 \gg 1$, and $A - B\omega^2 \approx B\omega^2$, (17) can be expressed as

$$|G_{FO}(j\omega)| = \frac{1}{L_1 L_2 C_f \omega^\alpha} \frac{L_f C_f \omega^2}{\sqrt{\left(\omega^{\alpha + \beta_f} + B\omega^2 \cos \frac{(\alpha + \beta_f)\pi}{2}\right)^2 + B^2 \omega^4 \sin^2 \frac{(\alpha + \beta_f)\pi}{2}}} \tag{25}$$

$$\omega_{t3} = \left| B \cos \frac{(\alpha + \beta_f)\pi}{2} \right|^{\frac{1}{\alpha + \beta_f}} \tag{26}$$

Define intermediate variables ω_{t3} and ω_{t4} as follows:

$$\omega_{t4} = \left| B \sin \frac{(\alpha + \beta_f)\pi}{2} \right|^{\frac{1}{\alpha + \beta_f}} \tag{27}$$

Substitute (26) and (27) into (25); the magnitude–frequency characteristic can be derived as

$$|G_{FO}(j\omega)| = \frac{1}{L_1 L_2 C_f \omega^\alpha} \frac{L_f C_f \omega^2}{\sqrt{(\omega^{\alpha + \beta_f} + \tau \omega_{t3}^{\alpha + \beta_f})^2 + \omega_{t4}^{2(\alpha + \beta_f)}}} \tag{28}$$

When $\omega \gg \omega_{rp1}$ and $\alpha + \beta_f \in [2, 4)$, $\omega^2(\omega_{t3}/\omega)^{\alpha + \beta_f} \approx 0$, and $\omega^2(\omega_{t4}/\omega)^{\alpha + \beta_f} \approx 0$, (17) can be expressed as

$$|G_{FO}(j\omega)| = \frac{1}{L_1 L_2 C_f \omega^{2\alpha + \beta_f}} \frac{L_f C_f \omega^2}{\sqrt{\left(1 + \tau \omega^2 (\omega_{t3}/\omega)^{\alpha + \beta_f}\right)^2 + \omega^4 (\omega_{t4}/\omega)^{2(\alpha + \beta_f)}}} \approx \frac{L_f}{L_1 L_2 \omega^{2\alpha + \beta_f - 2}} \quad (29)$$

The log magnitude–frequency characteristics and the slope of its asymptote are expressed as (30) and (31).

$$L(\omega) \approx 20 \lg L_f - 20 \lg(L_1 L_2) - 20(2\alpha + \beta_f - 2) \lg \omega \quad (30)$$

$$\frac{dL(\omega)}{d \lg \omega} \approx -20(2\alpha + \beta_f - 2) \text{ dB/dec}, \omega \gg \omega_{rp1} \quad (31)$$

Similarly, when $\omega \gg \omega_{rp1}$ and $\alpha + \beta_f \in (0, 2)$, the slope of the asymptote is -20α dB/dec.

Theorem 2. For FOLLCL, when $\omega \ll \omega_{rp2}$, the asymptote slope of the low-frequency log magnitude–frequency characteristic is -20α dB/dec. When $\omega \gg \omega_{rp1}$, $\alpha + \beta_f \in [2, 4)$, the asymptote slope of the high-frequency log magnitude–frequency characteristics is $-20(2\alpha + \beta_f - 2)$ dB/dec; if $\alpha + \beta_f \in (0, 2)$, the asymptote slope is -20α dB/dec.

3.3. Phase–Frequency Characteristic

According to (6), when $\alpha_f + \beta_f = 2$, the phase model can be expressed as

$$\angle G_{FO}(j\omega) = -\arctan\left(\tan \frac{\pi\alpha}{2}\right) - \arctan \frac{\omega^{\alpha + \beta_f} \sin \frac{(\alpha + \beta_f)\pi}{2}}{\omega^{\alpha + \beta_f} \cos \frac{(\alpha + \beta_f)\pi}{2} + A - B\omega^2} \quad (32)$$

(1) When $\omega \ll \omega_{rp1}$, $A - B\omega^2 \approx A$ and $\omega^{\alpha + \beta_f} \sin[(\alpha + \beta_f)\pi/2] \ll \omega^{\alpha + \beta_f} \cos[(\alpha + \beta_f)\pi/2] + A$, so the low-frequency phase is expressed as

$$\angle G_{FO}(j\omega) \approx -\arctan\left(\tan \frac{\pi\alpha}{2}\right) - \arctan \frac{\omega^{\alpha + \beta_f} \sin \frac{(\alpha + \beta_f)\pi}{2}}{\omega^{\alpha + \beta_f} \cos \frac{(\alpha + \beta_f)\pi}{2} + A} \approx -\frac{\pi\alpha}{2} \quad (33)$$

(2) When $\omega \gg \omega_{rp1}$, $A - B\omega^2 \approx -B\omega^2$ and $B\omega^2 \ll |\omega^{\alpha + \beta_f} \cos[(\alpha + \beta_f)\pi/2]|$. Moreover, when $\alpha + \beta_f \in [2, 4)$, $\arctan\left\{\tan[(\alpha + \beta_f)\pi/2]\right\} = (\alpha + \beta_f)\pi/2 - 2\pi$, so the high-frequency phase is expressed as

$$\begin{aligned} \angle G_{FO}(j\omega) &\approx \pi - \arctan\left(\tan \frac{\pi\alpha}{2}\right) - \arctan \frac{\omega^{\alpha + \beta_f} \sin \frac{(\alpha + \beta_f)\pi}{2}}{\omega^{\alpha + \beta_f} \cos \frac{(\alpha + \beta_f)\pi}{2} - B\omega^2} \\ &\approx \pi - \arctan\left(\tan \frac{\pi\alpha}{2}\right) - \arctan \frac{\omega^{\alpha + \beta_f} \sin \frac{(\alpha + \beta_f)\pi}{2}}{\omega^{\alpha + \beta_f} \cos \frac{(\alpha + \beta_f)\pi}{2}} = -\pi(\alpha + \beta_f/2) + \pi \end{aligned} \quad (34)$$

When $\alpha + \beta_f \in (0,2)$, $\omega^{\alpha+\beta_f} \sin[(\alpha + \beta_f)\pi/2] \ll |\omega^{\alpha+\beta_f} \cos[(\alpha + \beta_f)\pi/2] - B\omega^2|$, so the high-frequency phase can be expressed as

$$\angle G_{FO}(j\omega) \approx -\arctan\left(\tan \frac{\pi\alpha}{2}\right) - \arctan \frac{\omega^{\alpha+\beta_f} \sin \frac{(\alpha + \beta_f)\pi}{2}}{\omega^{\alpha+\beta_f} \cos \frac{(\alpha + \beta_f)\pi}{2} - B\omega^2} \approx -\frac{\pi\alpha}{2} \quad (35)$$

Theorem 3. For FOLLCL, when $\omega \ll \omega_{rp2}$, the low-frequency phase is $-\pi\alpha/2$. When $\omega \gg \omega_{rp1}$, if $\alpha + \beta_f \in [2, 4)$, the high-frequency phase is $-\pi(\alpha + \beta_f/2) + \pi$; if $\alpha + \beta_f \in (0, 2)$, the high-frequency phase is $-\pi\alpha/2$.

It can be seen from Theorem 2 and Theorem 3 that the low-frequency characteristics only depend on the orders of L_1 and L_2 , and are independent of the orders of L_f and C_f . The high-frequency characteristics are determined by the orders of L_1 , L_2 , and C_f when $\alpha + \beta_f \in [2, 4)$, and only depend on the orders of L_1 and L_2 when $\alpha + \beta_f \in (0, 2)$.

3.4. Simulation Analyses

The bode plots of the FOLLCL filter are shown in Figure 4. The specific parameters of the FOLLCL filter are given in Table 1. Two cases are considered, namely, $\alpha + \beta_f \leq 2$ and $\alpha + \beta_f \geq 2$. The values of the asymptote slopes and phases are marked in the plots; it can be seen that the results are consistent with the theoretical analyses. In particular, the positive resonance peak is suppressed when $\alpha + \beta_f \neq 2$. Furthermore, it is shown in Figure 4b that when $\alpha + \beta_f > 2$, the phase-frequency characteristic curves do not pass through -180° , which means that the phase crossover frequency does not exist. Therefore, $\alpha + \beta_f$ must be less than or equal to 2 to guarantee the stability.

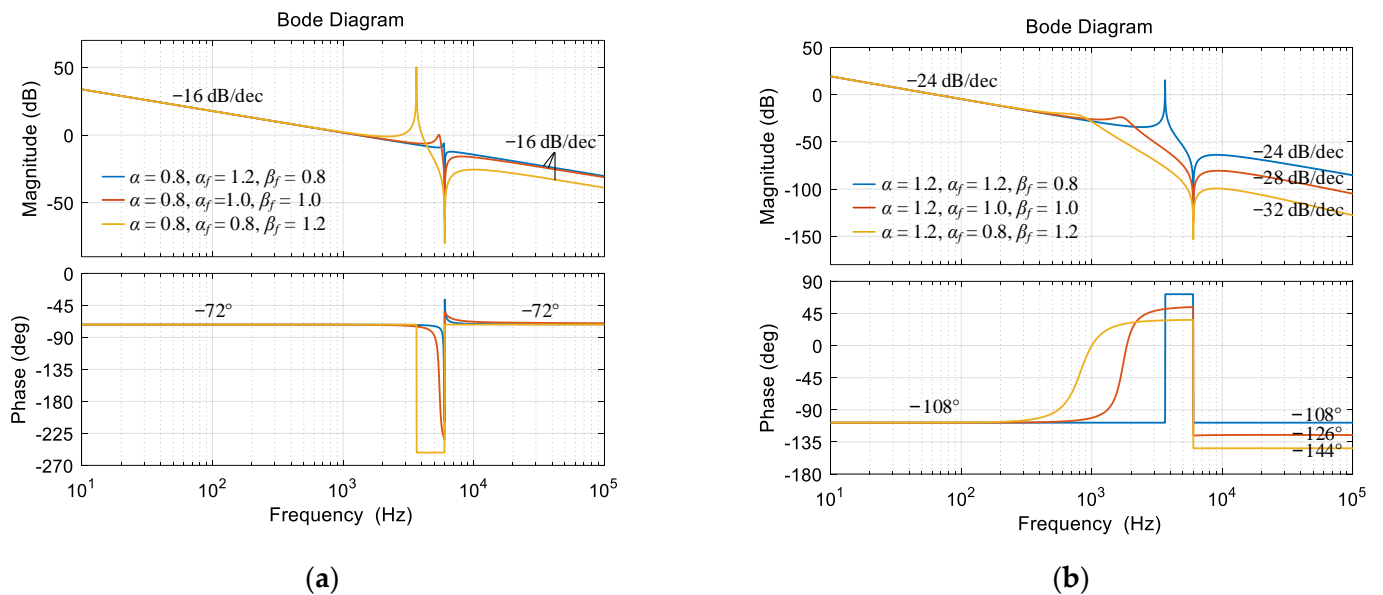


Figure 4. Bode diagrams of the FOLLCL filter. (a) $\alpha = 0.8, \alpha + \beta_f \leq 2$, (b) $\alpha = 1.2, \alpha + \beta_f \geq 2$.

4. Grid-Tied Inverter Based on Fractional-Order LLCL Filter

An FOLLCL filter and a VSI can be combined to form a grid-tied inverter. Figure 5 shows the single-phase FOLLCL-type grid-tied inverter and its control system. The primary objective of the grid-tied inverter is to control the grid-side current i_g to be synchronized with the grid voltage, which is denoted by u_g . I^* is the reference amplitude of the grid-side current, θ is the phase of grid voltage obtained by the phase-locked loop (PLL), and

i_g^* is the reference of the grid-side current. i_g is sensed with the sensor gain of H_{ig} and compared with i_g^* . The current error is sent to the current regulator G_i ; $G_i = K_p + K_i/s^\lambda$, and K_p , K_i , and λ are the proportional coefficient, integral coefficient, and order of the integrator, respectively. For the FOLLCL filter with $\alpha + \beta_f$ equaling or very close to 2, an active damping method is used to attenuate the positive resonance. The output of G_i is sent to the PWM generator after subtracting the capacitor current i_C , which is sensed with the sensor gain of H_{iC} . For the FOLLCL filter with $\alpha + \beta_f$ deviating from 2, the output of G_i is sent to the PWM generator directly; the active damping can be avoided.

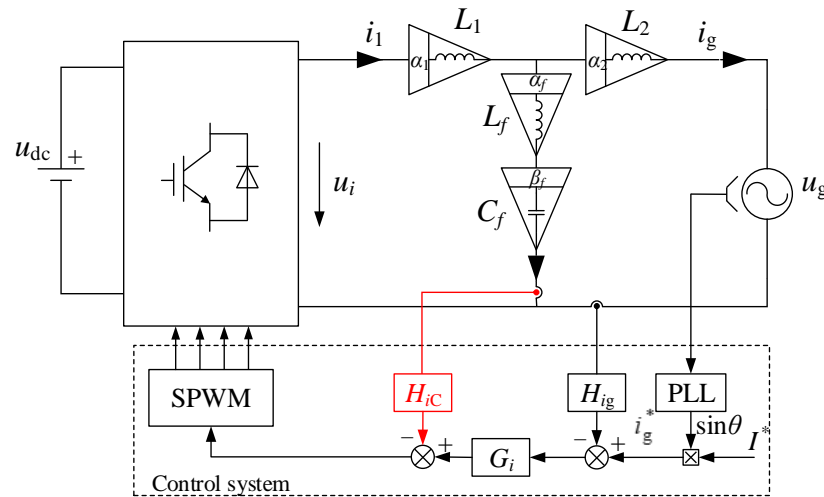


Figure 5. Single-phase FOLLCL-type grid-tied inverter and its control system.

4.1. Structure of the Control System

According to Figure 5, the control block diagram of the single-phase FOLLCL-type grid-tied inverter when $\alpha + \beta_f$ equals to or is very close to 2 is shown in Figure 6, where K_{PWM} is the transfer function from the modulation signal to the inverter output voltage, expressed as $K_{PWM} = u_{dc}/V_{tri}$, and V_{tri} is the amplitude of triangular carrier. $Z_{L1}(s)$, $Z_{L2}(s)$, $Z_{Lf}(s)$, and $Z_{Cf}(s)$ are the impedance of L_1 , L_2 , L_f , and C_f , respectively, which are expressed as

$$Z_{L1}(s) = s^\alpha L_1, \quad Z_{L2}(s) = s^\alpha L_2, \quad Z_{Lf}(s) = s^{\alpha_f} L_f, \quad Z_{Cf}(s) = 1/s^{\beta_f} C_f \quad (36)$$

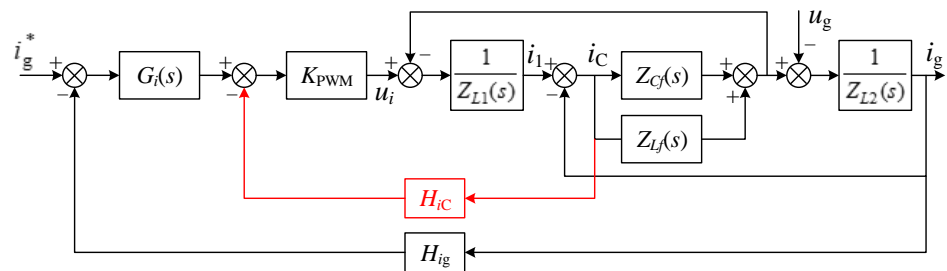


Figure 6. Control block diagram of single-phase FOLLCL-type grid-tied inverter when $\alpha + \beta_f$ equals or very close to 2.

The control block diagram of the single-phase FOLLCL-type grid-tied inverter when $\alpha + \beta_f$ deviates from 2 is shown in Figure 7. Compared with Figure 6, the capacitor current feedback loop is removed.

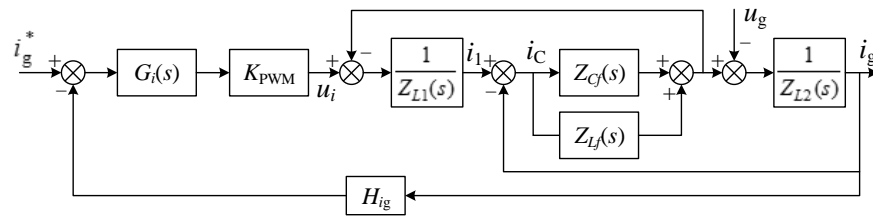


Figure 7. Control block diagram of single-phase FOLLCL-type grid-tied inverter when $\alpha + \beta_f$ deviates from 2.

The control block diagrams in Figures 6 and 7 can be equivalently transformed into the block diagram in Figure 8. The transfer functions G_{x1} and G_{x2} are expressed as (37) and (38), respectively:

$$G_{x1}(s) = \frac{K_{PWM}G_i(s) [Z_{Lf}(s) + Z_{Cf}(s)]}{Z_{L1}(s) + Z_{Lf}(s) + Z_{Cf}(s) + H_{iC}K_{PWM}} \tag{37}$$

$$G_{x2}(s) = \frac{Z_{L1}(s) + Z_{Lf}(s) + Z_{Cf}(s) + H_{iC}K_{PWM}}{Z_{L1}(s)Z_{L2}(s) + [Z_{L1}(s) + Z_{L2}(s)] [Z_{Lf}(s) + Z_{Cf}(s)] + H_{iC}K_{PWM}Z_{L2}(s)} \tag{38}$$

where $H_{iC} = 0$ when $\alpha + \beta_f \neq 2$.

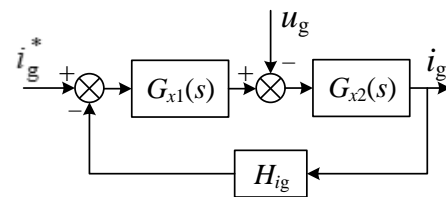


Figure 8. Equivalent block diagram of Figures 6 and 7.

According to the equivalent block diagram in Figure 8 and (36)~(38), the expression of the loop gain can be derived as

$$T_A(s) = G_{x1}(s)G_{x2}(s)H_{ig}(s) = \frac{H_{ig}K_{PWM}G_i(s) (L_f C_f s^{\alpha_f + \beta_f} + 1)}{L_1 L_2 C_f s^{2\alpha + \beta_f} + (L_1 + L_2)L_f C_f s^{\alpha + \alpha_f + \beta_f} + L_2 C_f H_{iC} K_{PWM} s^{\alpha + \beta_f} + (L_1 + L_2)s^\alpha} \tag{39}$$

As discussed in Part 3, $\alpha_f + \beta_f = 2$ must be satisfied in grid-tied inverter applications, so (39) is rewritten as

$$T_A(s) = \frac{H_{ig}K_{PWM}G_i(s) (L_f C_f s^2 + 1)}{L_1 L_2 C_f s^{2\alpha + \beta_f} + (L_1 + L_2)L_f C_f s^{\alpha + 2} + L_2 C_f H_{iC} K_{PWM} s^{\alpha + \beta_f} + (L_1 + L_2)s^\alpha} \tag{40}$$

The grid current i_g can be expressed as

$$i_g(s) = \frac{1}{H_{ig}} \frac{T_A(s)}{1 + T_A(s)} i_g^*(s) - \frac{G_{x2}(s)}{1 + T_A(s)} u_g(s) = i_{g1}(s) + i_{g2}(s) \tag{41}$$

It can be seen from (41) that $i_g(s)$ consists of two parts: the reference tracking component $i_{g1}(s)$ and the disturbance component $i_{g2}(s)$ caused by the grid voltage, which can be expressed as (42) and (43), respectively.

$$i_{g1}(s) = \frac{1}{H_{ig}} \frac{T_A(s)}{1 + T_A(s)} i_g^*(s) \tag{42}$$

$$i_{g2}(s) = -\frac{G_{x2}(s)}{1 + T_A(s)} u_g(s) \quad (43)$$

4.2. System Performance Analysis

The loop gain at the fundamental frequency is often much greater than one, so $1 + T_A(s) \approx T_A(s)$, and (42) can be rewritten as $i_{g1}(s) \approx i_g^*(s)/H_{ig}$. Therefore, $i_{g1}(s)$ and $i_g^*(s)$ are almost in phase. For $f \leq f_c$, the $L_f - C_f$ branch can be considered open. According to (38) and (40), the expression of $G_{x2}(s)$ and $T_A(s)$ at the fundamental frequency can be obtained as follows:

$$G_{x2}(j2\pi f_o) \approx \frac{1}{(j2\pi f_o)^\alpha (L_1 + L_2)} \quad (44)$$

$$T_A(j2\pi f_o) \approx \frac{H_{ig} K_{PWM} G_i(j2\pi f_o)}{(j2\pi f_o)^\alpha (L_1 + L_2)} \quad (45)$$

where f_o is the fundamental frequency. Substitute (44) and (45) into (43), and for PI regulator, $G_i(j2\pi f_o) \approx K_i/(j2\pi f_o)$, so we have

$$i_{g2} \approx -\frac{u_g}{H_{ig} K_{PWM} G_i(j2\pi f_o)} \approx -\frac{j2\pi f_o u_g}{H_{ig} K_{PWM} K_i} \quad (46)$$

From (46), it can be seen that i_{g2} lags behind u_g by 90° ; a small i_{g2} is expected to reduce the amplitude and phase tracking errors for i_g . From (45) and (46), the RMS value of i_{g2} can be expressed as

$$I_{g2} \approx \frac{U_g}{H_{ig} K_{PWM} |G_i(j2\pi f_o)|} \approx \frac{U_g}{(2\pi f_o)^\alpha (L_1 + L_2) |T_A(j2\pi f_o)|} \quad (47)$$

The magnitude of the loop gain at f_o is expressed as

$$T_{fo} = 20 \lg \left| T_A(j2\pi f_o) \right| \approx 20 \lg \frac{U_g}{(2\pi f_o)^\alpha (L_1 + L_2) I_{g2}} \quad (48)$$

where the unit of T_{fo} is dB. Thus, the steady-state error requirement for I_{g2} is converted to the requirement for T_{fo} . Obviously, for a given value of I_{g2} , a smaller-order α means bigger T_{fo} .

Compared to the PI regulator, the PR regulator can significantly increase T_{fo} , and thus decrease the steady-state error of the grid current. The expression of the PR regulator is

$$G_i(s) = K_p + \frac{2K_r \omega_i s}{s^2 + 2\omega_i s + \omega_o^2} \quad (49)$$

where K_p is the proportional coefficient, K_r is the resonant coefficient, ω_i is the bandwidth concerning the -3 dB cutoff frequency of the resonant compensator, and $\omega_o = 2\pi f_o$ is the fundamental angular frequency. The design criteria of the PR regulator have been reported in many works in the literature and will not be repeated here.

In order to demonstrate the control system design criteria of the FOLLCL-type grid-tied inverter, four cases are presented based on the system parameters listed in Tables 1 and 2.

Case I ($\alpha + \beta_f = 2$, PI control): For $\alpha + \beta_f = 2$ (taking $(\alpha, \alpha_f, \beta_f) = (1.2, 1.2, 0.8)$ and $(\alpha, \alpha_f, \beta_f) = (1.1, 1.1, 0.9)$ as examples), the bode diagrams of the loop gain before compensation ($G_i(s) = 1$) are drawn in Figure 9 according to (40), where f_c is the cut-off frequency of the loop gain. As shown in Figure 9, the capacitor current feedback can effectively suppress the positive resonance peak of the FOLLCL filter, and the resonance damping capability becomes stronger with the increase of H_{iC} . As with the application in conventional IOLCL-type grid-tied inverters, this well-known active damping method only changes the

magnitude–frequency characteristics around the resonant frequency f_{rp2} . However, the phase–frequency characteristics vary observably; they decrease from $-(90\alpha)^\circ$ when $f < f_{rp2}$.

Table 2. System Parameters.

Parameter	Symbol	Value
DC voltage	u_{dc}	360 V
grid voltage (RMS)	U_g	220 V
fundamental frequency	f_o	50 Hz
switching frequency	f_s	3 kHz
amplitude of the triangular carrier	V_{tri}	3.05 V

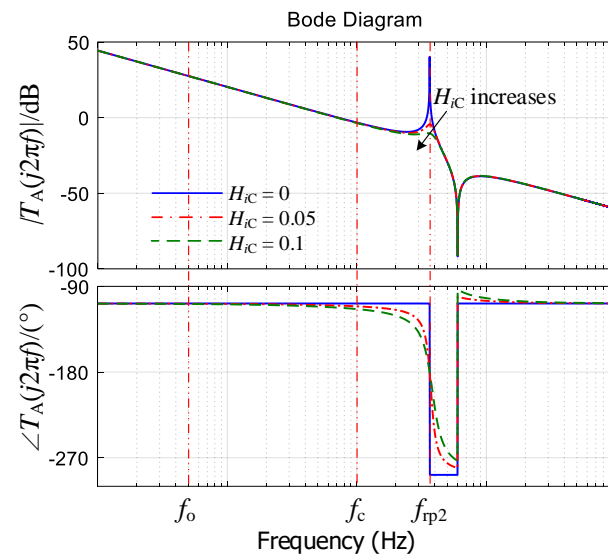


Figure 9. Bode diagrams of the loop gain before compensation when $\alpha + \beta_f = 2$.

The control system parameter design principles for IOLCL-type grid-tied inverters are adopted here to control the FOLLCL-type grid-tied inverter with $\alpha + \beta_f = 2$. The bode diagrams of the loop gain after compensation ($G_i(s) = K_p + K_i/s$) are shown in Figure 10. The frequency characteristics without active damping and compensation (green dotted lines) when $(\alpha, \alpha_f, \beta_f) = (1.2, 1.2, 0.8)$ are also plotted in the same figure for comparison purpose. $H_{iC} = 0.1$, $H_{ig} = 0.15$, $K_p = 0.45$, and $K_i = 2200$ are designed in this case to yield a satisfactory overall system performance. Compared with the original system (green dotted lines), the loop gain at the fundamental frequency (T_{f_0}) after compensation (blue solid lines) increases and the high-frequency ($f > f_{rp1}$) magnitude characteristics move down, which can guarantee the fundamental current tracking and high-frequency harmonic attenuation capabilities. It can also be seen from Figure 10 that a lower α can guarantee better performance under the condition of $\alpha + \beta_f = 2$. When $\alpha = 1.1$, the system has a sufficient gain margin ($GM = 5.04$ dB) and an acceptable phase margin ($PM = 38.1^\circ$, while $PM > 45^\circ$ is required for a well-designed system), as well as a reasonable cut-off frequency ($f_c = 948$ Hz) and a sufficient fundamental loop gain ($T_{f_0} = 49.5$ dB), while when $\alpha = 1.2$, although there is a slightly higher gain margin ($GM = 5.74$ dB), the PM , f_c , and T_{f_0} all decrease. The low phase margin ($PM = 17.1^\circ$) especially threatens the system stability.

Case II ($\alpha + \beta_f \neq 2$, PI control): For $\alpha + \beta_f \neq 2$ (taking $\alpha = 1.1$, $\alpha_f = 1.2$, $\beta_f = 0.8$ as an example), the bode diagrams of the loop gain before compensation ($G_i(s) = 1$) are drawn in Figure 11. $H_{iC} = 0$ is set in this case to avoid active damping. The positive resonance peak is damped effectively by selecting appropriate values for orders α and β_f to make their sum unequal to 2. When $H_{ig} = 0.15$, the same value as in case I, the cut-off frequency is very close to the equivalent switching frequency $2f_s$ (6 kHz), which is not acceptable for a grid-tied inverter. Moreover, when $H_{ig} = 0.1$ or 0.15 , the magnitude plot has three

cut-off frequencies and the system behaves as a conditionally stable system. For a large H_{ig} , even if the system can be stable after compensation, it is not easy to obtain a sufficient gain margin. If we keep decreasing H_{ig} to 0.05, the magnitude plot has only one cut-off frequency. Therefore, $H_{ig} = 0.05$ is chosen for the compensated system in the next step.

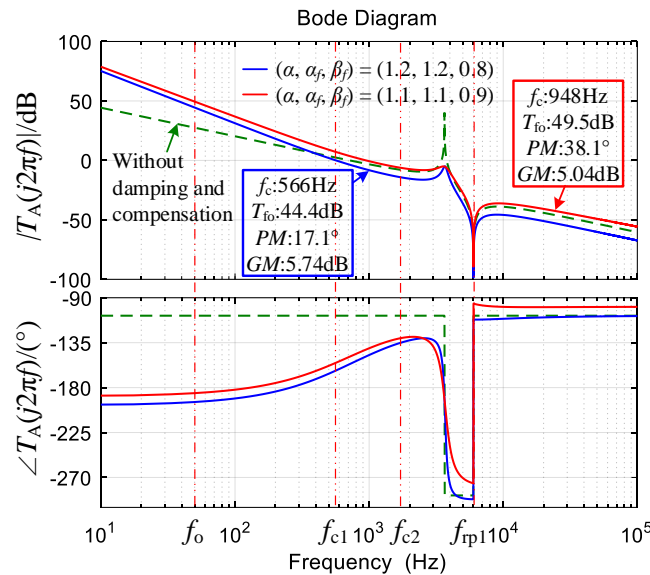


Figure 10. Bode diagrams of the loop gain after compensation when $\alpha + \beta_f = 2$.

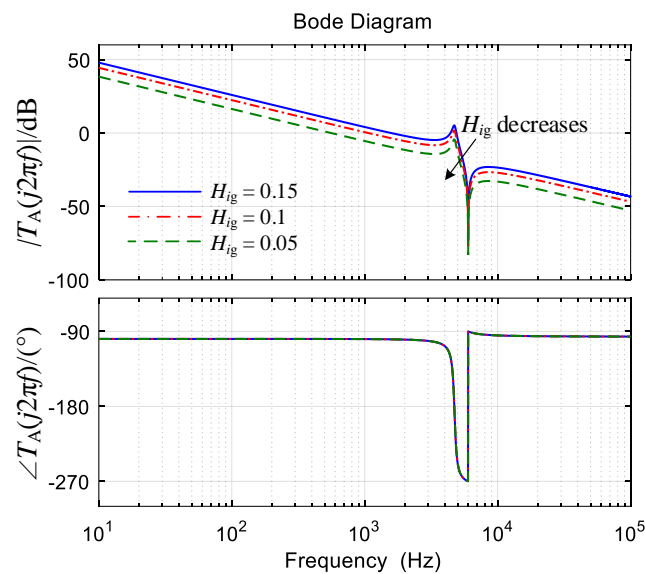


Figure 11. Bode diagrams of the loop gain before compensation when $\alpha + \beta_f \neq 2$.

The bode diagrams of the loop gain after compensation ($G_i(s) = K_p + K_i/s^\lambda$, $\lambda = 1$) are shown in Figure 12. As seen from (46), the decrease of H_{ig} will increase i_{g2} , so K_i should be increased to meet the steady-state error requirement. However, the phase margin when $K_i = 2200$ is only 22.7° , and after increasing K_i from 2200 to 4000, the phase margin decreases to 14.6° , and a sufficient phase margin cannot be guaranteed.

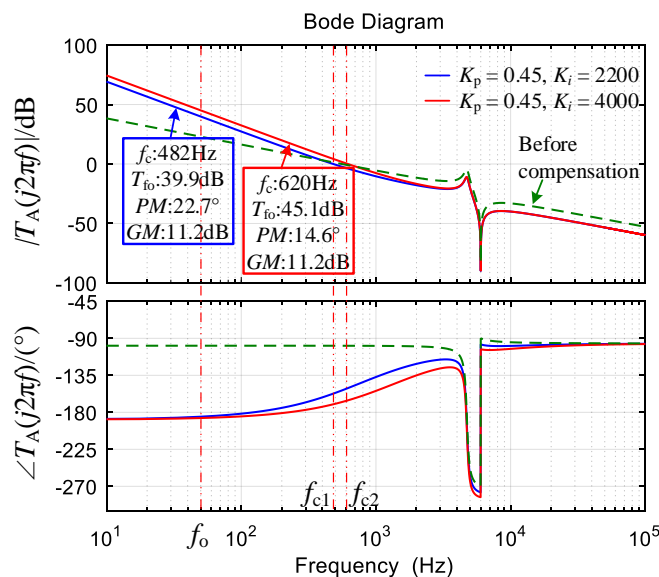


Figure 12. Bode diagrams of the loop gain after compensation with a PI controller when $\alpha + \beta_f \neq 2$ (varying K_i).

Case III ($\alpha + \beta_f \neq 2$, PI^λ control): In this case, $(\alpha, \alpha_f, \beta_f) = (1.1, 1.2, 0.8)$, $H_{iC} = 0$, $H_{ig} = 0.05$, and a fractional-order PI^λ regulator is used to try to improve the phase margin. When $K_p = 0.45$, $K_i = 2200$, and λ increases from 0.8 to 1.4, the bode diagrams of the loop gain are shown in Figure 13. The phase margin increases with λ , so $\lambda = 1.4$ is selected to leave enough room for K_i adjustment.

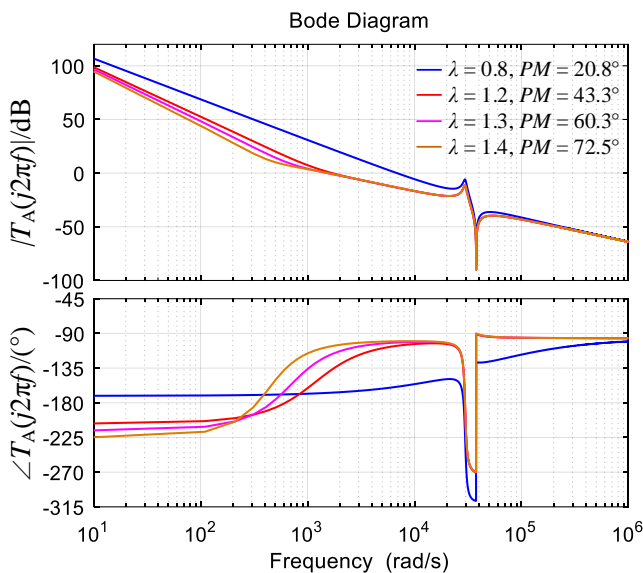


Figure 13. Bode diagrams of the loop gain after compensation with a PI^λ controller when $\alpha + \beta_f \neq 2$ (varying λ).

The bode diagrams of the loop gain with varying K_i when $\lambda = 1.4$ are shown in Figure 14. With the increase of K_i , the phase margin decreases, but it is still sufficient even $K_i = 6000$ ($PM = 49.2^\circ$). However, each curve in Figures 13 and 14 has a small T_{fo} , so the steady-state error requirement is still not guaranteed according to (47) and (48). The contradiction between T_{fo} and PM cannot be balanced by a PI^λ regulator.

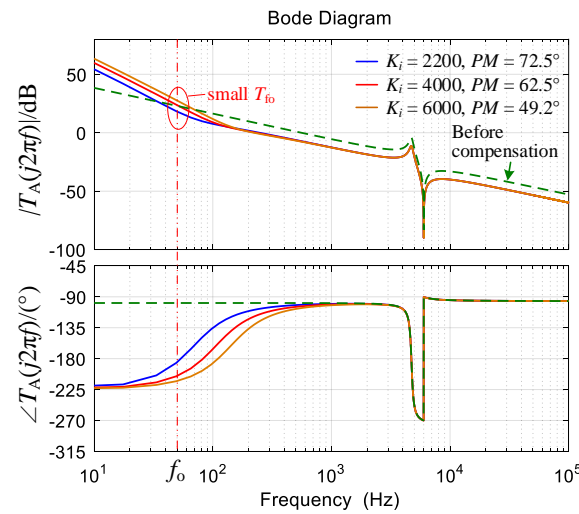


Figure 14. Bode diagrams of the loop gain after compensation with a PI^λ controller when $\alpha + \beta_f \neq 2$ ($\lambda = 1.4$ and varying K_i).

Case IV ($\alpha + \beta_f \neq 2$, PR control): In this case, $(\alpha, \alpha_f, \beta_f) = (1.1, 1.2, 0.8)$, $H_{iC} = 0$, $H_{ig} = 0.05$, and a PR regulator is used to control the grid current. The values of the parameters are $K_p = 0.45$, $\omega_o = 2\pi \times 50$ rad/s, and $\omega_i = \pi$ rad/s, and K_r increases from 100 to 300; the bode diagrams of the compensated system are shown in Figure 15. It can be seen that each curve has a large enough T_{fo} to eliminate the steady-state error of i_g . However, PM decreases with the increase of K_r , when $K_r = 100$, $GM = 11.3$ dB, PM is 59.3° , and the f_c also has a good value, so $K_r = 100$ will be selected in the simulation section.

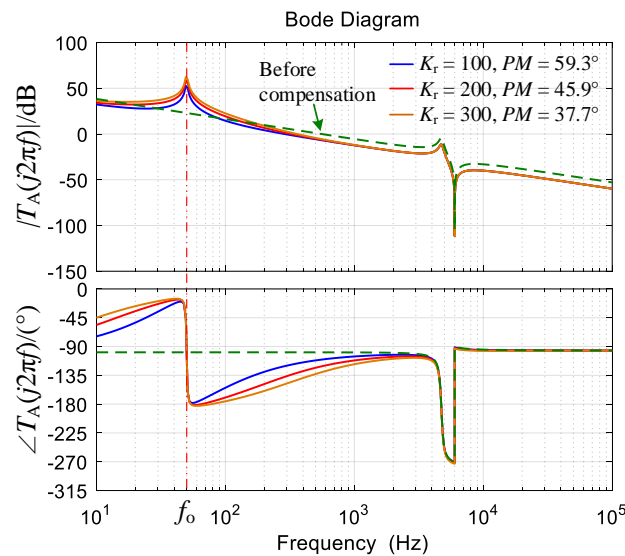


Figure 15. Bode diagrams of the loop gain after compensation with a PR controller when $\alpha + \beta_f \neq 2$ (varying K_r).

Based on the four cases discussed previously, it can be concluded that:

- (1) If $\alpha + \beta_f = 2$, the FOLLCL-type grid-tied inverter can be damped by a capacitor current feedback loop. Under PI control, a lower α can achieve a larger PM but a higher f_c .
- (2) If $\alpha + \beta_f \neq 2$, the system is stable under the grid current feedback; the capacitor current feedback is avoided. Under PI control, a large K_i should be chosen to reduce the steady-state error of i_g , but the PM decreases significantly.
- (3) A PI^λ regulator can also make the system stable, but there is a contradiction between T_{fo} and PM .

- (4) A PR regulator can simultaneously obtain good T_{fo} , GM , PM , and f_c , which is suitable for controlling the FOLLCL-type grid-tied inverter if $\alpha + \beta_f \neq 2$.

5. Simulations

To verify the characteristics of the FOLLCL-type grid-tied inverter and the effectiveness of the control methods, simulations are conducted with the parameters presented in Tables 1 and 2. In each simulation, the reference grid current i_g^* is set to $50\sin(\omega t)$ A; i_g is magnified three times for observation in the waveform diagram. The fractional-order inductors and capacitor are equivalent to the fractance circuit using the Oustaloup approximation method. In the first simulation, an IOLCL-type grid-tied inverter is studied. As shown in Figure 16, a large amount of harmonics, which is mainly around $2f_s$ (6 kHz), exists in the grid current. The THD of i_g is 14.46%, which is not acceptable in the application. The result indicates that the LCL-type grid-tied inverter has little advantage in low-frequency applications.

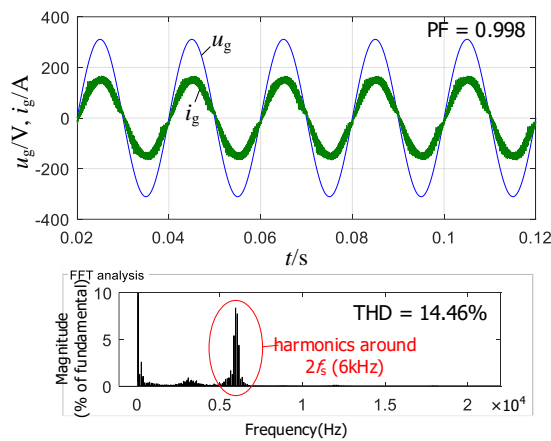


Figure 16. Simulation results of the IOLCL-type grid-tied inverter.

In the second simulation, an FOLLCL-type grid-tied inverter with $\alpha + \beta_f = 2$ and $\alpha_f + \beta_f = 2$ ($\alpha = 1.1, \alpha_f = 1.1, \beta_f = 0.9$) under PI control is investigated. As shown in Figure 17, when the capacitor current feedback loop is effective before 0.1 s, the system is stable, the grid current has a very low THD (only 0.26%), and the power factor is high (0.998). The FOLLCL-type grid-tied inverter exhibits excellent harmonic suppression ability. However, instability arises after 0.1 s due to the removal of the capacitor current feedback loop, which causes positive resonance.

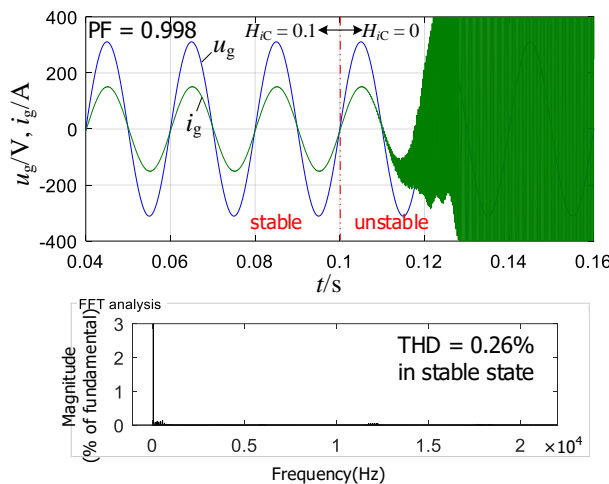


Figure 17. Simulation results of the FOLLCL-type grid-tied inverter with $\alpha + \beta_f = 2$ and a PI regulator.

Moreover, an FOLLCL-type grid-tied inverter with $\alpha + \beta_f \neq 2$ and $\alpha_f + \beta_f = 2$ ($\alpha = 1.1$, $\alpha_f = 0.2$, $\beta_f = 0.8$) is studied. The inverter is regulated by a PI controller; the control parameters are $K_p = 0.45$ and $K_i = 2200$, respectively. As with the analysis in Section 4 (case II), the capacitor current feedback is eliminated and $H_{ig} = 0.05$. As shown in Figure 18, the system is stable without active damping and the grid current is close to the ideal sine, which has a THD of 0.72%. However, to obtain a sufficient phase margin, K_i cannot be too large, resulting in a certain phase error between u_g and i_g ; the power factor is only 0.989.

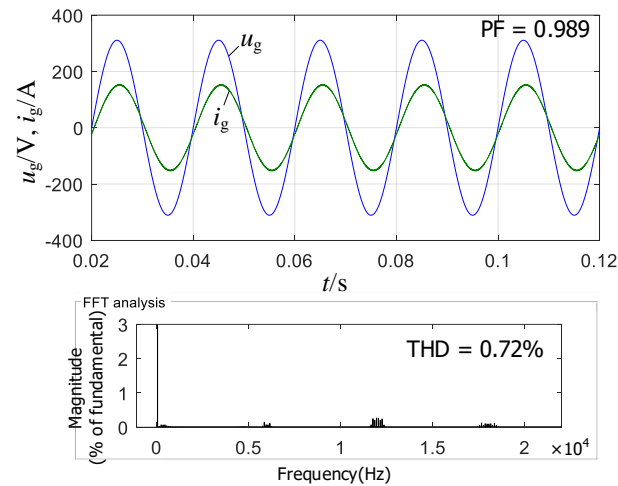


Figure 18. Simulation results of the FOLLCL-type grid-tied inverter with $\alpha + \beta_f \neq 2$ and a PI regulator.

Furthermore, in Figure 19, the simulation results of the FOLLCL-type grid-tied inverter with $\alpha + \beta_f \neq 2$ and $\alpha_f + \beta_f = 2$ ($\alpha = 1.1$, $\alpha_f = 1.2$, $\beta_f = 0.8$) controlled by a PI^λ regulator are shown. According to the analysis in Section 4 and case III, when $\lambda = 1.4$ and $K_i = 6000$, although $PM > 45^\circ$, the T_{fo} is very small, as can be seen in Figure 14. Therefore, as shown in Figure 19, both the amplitude error and phase error between i_g^* and i_g are very large, and the power factor is only 0.906.

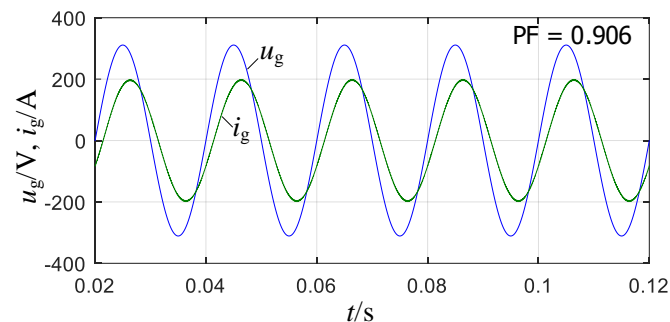


Figure 19. Simulation results of the FOLLCL-type grid-tied inverter with $\alpha + \beta_f \neq 2$ and a PI^λ regulator.

Finally, a PR regulator is used to control the FOLLCL-type grid-tied inverter with $\alpha + \beta_f \neq 2$ and $\alpha_f + \beta_f = 2$ ($\alpha = 1.1$, $\alpha_f = 1.2$, $\beta_f = 0.8$). $K_p = 0.45$, $\omega_i = \pi$, and $K_r = 100$ are the parameters of the regulator, and $H_{ig} = 0.05$. The results are shown in Figure 20. The grid current is in strict in-phase with the grid voltage; the power factor is 1. In addition, the amplitude error is close to 0. The results are consistent with the previous analysis in Section 4.

The above simulation results prove that the analyses in previous sections are correct and PR regulator is superior to PI and PI^λ regulators to control an FOLLCL-type grid-tied inverter with $\alpha + \beta_f \neq 2$.

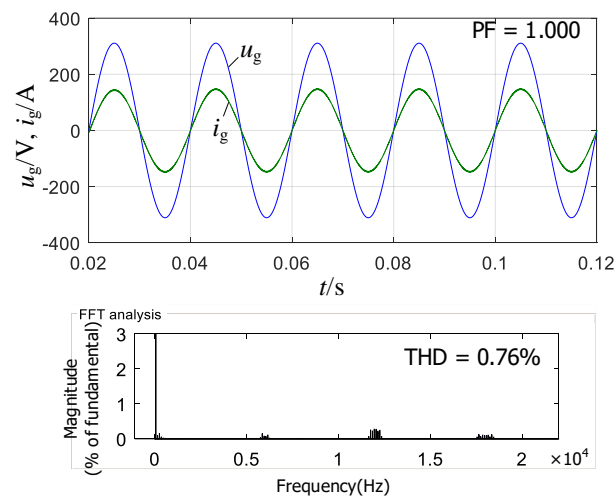


Figure 20. Simulation results of the FOLLCL-type grid-tied inverter with $\alpha + \beta_f \neq 2$ and a PR regulator.

6. Conclusions

In this paper, the fractional-order LLCL filter and the grid-tied inverter based on it are studied. By correctly selecting the orders of the components, the positive resonance can be suppressed and the negative resonance is reserved. Therefore, the passive or active damping can be avoided for the FOLLCL-type grid-tied inverter. Meanwhile, the switching-frequency harmonics in the grid current can be attenuated. For low-frequency applications, it is difficult for the PI controller and fractional-order PI controller to balance all performances simultaneously. PR controllers can guarantee good fundamental frequency loop gain, cut-off frequency, gain margin, and phase margin at the same time. The FOLLCL-type grid-tied inverter without active damping under PR control achieves excellent tracking accuracy and low grid current THD. Simulations are conducted to verify the correctness of the theoretical analyses.

Author Contributions: Methodology, X.W.; Software, R.Z. and J.C.; Validation, R.Z. and J.C.; Investigation, X.W.; Writing—original draft, X.W.; Writing—review & editing, X.W. All authors have read and agreed to the published version of the manuscript.

Funding: This work was supported by the “Guangzhou Science and Technology Plan Project, no. 202102010404”.

Institutional Review Board Statement: Not applicable.

Informed Consent Statement: Not applicable.

Data Availability Statement: Not applicable.

Conflicts of Interest: The authors declare no conflict of interest.

References

1. Twining, E.; Holmes, D.G. Grid current regulation of a three-phase voltage source inverter with an LCL input filter. *IEEE Trans. Power Electron.* **2003**, *18*, 888–895. [\[CrossRef\]](#)
2. Pan, D.H.; Ruan, X.B.; Wang, X.H.; Yu, H.; Xing, Z.W. Analysis and design of current control schemes for LCL-type grid-connected inverter based on a general mathematical model. *IEEE Trans. Power Electron.* **2017**, *32*, 4395–4410. [\[CrossRef\]](#)
3. Jayalath, S.; Hanif, M. Generalized LCL-filter design algorithm for grid-connected voltage-source inverter. *IEEE Trans. Ind. Electron.* **2017**, *64*, 1905–1915. [\[CrossRef\]](#)
4. Wu, W.M.; Liu, Y.; He, Y.B.; Chung, H.S.H.; Liserre, M.; Blaabjerg, F. Damping methods for resonances caused by LCL-filter-based current-controlled grid-tied power inverters: An overview. *IEEE Trans. Ind. Electron.* **2017**, *64*, 7402–7413. [\[CrossRef\]](#)
5. Wang, J.G.; Yan, J.D.; Jiang, L.; Zou, J.Y. Delay-dependent stability of single-loop controlled grid-connected inverters with LCL filters. *IEEE Trans. Power Electron.* **2016**, *31*, 743–757. [\[CrossRef\]](#)
6. Wu, W.M.; He, Y.B.; Blaabjerg, F. An LLCL- power filter for single-phase grid-tied inverter. *IEEE Trans. Power Electron.* **2012**, *27*, 782–789. [\[CrossRef\]](#)

7. Wu, W.M.; He, Y.B.; Tang, T.H.; Blaabjerg, F. A new design method for the passive damped LCL and LLCL filter-based single-phase grid-tied inverter. *IEEE Trans. Ind. Electron.* **2013**, *60*, 4339–4350. [[CrossRef](#)]
8. Wu, W.M.; Sun, Y.J.; Huang, M.; Wang, X.F.; Wang, H.; Blaabjerg, F.; Liserre, M.; Chung, H.S.H. A robust passive damping method for LLCL-filter-based grid-tied inverters to minimize the effect of grid harmonic voltages. *IEEE Trans. Power Electron.* **2014**, *29*, 3279–3289. [[CrossRef](#)]
9. Zhang, Z.H.; Wu, W.M.; Shuai, Z.K.; Wang, X.F.; Luo, A.; Chung, H.S.; Blaabjerg, F. Principle and robust impedance-based design of grid-tied inverter with LLCL-filter under wide variation of grid-reactance. *IEEE Trans. Power Electron.* **2019**, *34*, 4362–4374. [[CrossRef](#)]
10. Liu, Y.T.; Jin, D.H.; Jiang, S.Q.; Liang, W.H.; Peng, J.C.; Lai, C.M. An active damping control method for the LLCL filter-based SiC MOSFET grid-connected inverter in vehicle-to-grid application. *IEEE Trans. Veh. Technol.* **2019**, *68*, 3411–3423. [[CrossRef](#)]
11. Khan, A.; Gastli, A.; Ben-Brahi, L. Modeling and control for new LLCL filter based grid-tied PV inverters with active power decoupling and active resonance damping capabilities. *Electr. Power Syst. Res.* **2018**, *155*, 307–319. [[CrossRef](#)]
12. Attia, H.A.; Freddy, T.K.S.; Che, H.S.; El Khateb, A.H. Design of LLCL filter for single phase inverters with confined band variable switching frequency (CB-VSF) PWM. *J. Power Electron.* **2019**, *19*, 44–57.
13. Alemi, P.; Bae, C.; Lee, D. Resonance suppression based on PR control for single-phase grid-connected inverters with LLCL filters. *IEEE Trans. Emerg. Sel. Topics Power Electron.* **2016**, *4*, 459–467. [[CrossRef](#)]
14. Liu, Z.F.; Wu, H.Y.; Liu, Y.; Ji, J.H.; Wu, W.M.; Blaabjerg, F. Modelling of the modified-LLCL-filter-based single-phase grid-tied Aalborg inverter. *IET Power Electron.* **2017**, *10*, 151–1515. [[CrossRef](#)]
15. Miao, Z.Y.; Yao, W.X.; Lu, Z.Y. Single-cycle-lag compensator-based active damping for digitally controlled LCL/LLCL-type grid-connected inverters. *IEEE Trans. Ind. Electron.* **2020**, *63*, 1980–1990. [[CrossRef](#)]
16. Wang, F.Q.; Ma, X.K. Modeling and analysis of the fractional order Buck converter in DCM operation by using fractional calculus and the circuit-averaging technique. *J. Power Electron.* **2013**, *13*, 1008–1015. [[CrossRef](#)]
17. Jia, Z.R.; Liu, C.X. Fractional-order modeling and simulation of magnetic coupled boost converter in continuous conduction mode. *Int. J. Bifurc. Chaos* **2018**, *28*, 1850061. [[CrossRef](#)]
18. Yang, R.C.; Liao, X.Z.; Lin, D.; Dong, L. Modeling and analysis of fractional order Buck converter using Caputo–Fabrizio derivative. *Energy Rep.* **2020**, *6*, 440–445. [[CrossRef](#)]
19. Wei, Z.H.; Zhang, B.; Jiang, Y.W. Analysis and modeling of fractional-order buck converter based on Riemann-Liouville derivative. *IEEE Access* **2019**, *7*, 162768–162777. [[CrossRef](#)]
20. Xie, L.L.; Liu, Z.P.; Zhang, B. A modeling and analysis method for CCM fractional order Buck-boost converter by using R–L fractional definition. *J. Electr. Eng. Technol.* **2020**, *15*, 1651–1661. [[CrossRef](#)]
21. Chen, X.; Chen, Y.F.; Zhang, B.; Qiu, D.Y. A modeling and analysis method for fractional-order DC–DC converters. *IEEE Trans. Power Electron.* **2017**, *32*, 7034–7044. [[CrossRef](#)]
22. Radwan, A.G.; Emira, A.A.; AbdelAty, A.M.; Azar, A.T. Modeling and analysis of fractional order DC-DC converter. *ISA Trans.* **2018**, *82*, 184–199. [[CrossRef](#)] [[PubMed](#)]
23. Sharma, M.; Rajpurohit, B.S.; Agnihotri, S.; Rathore, A.K. Development of fractional order modeling of voltage source converters. *IEEE Access* **2020**, *8*, 131750–131759. [[CrossRef](#)]
24. Xu, J.H.; Li, X.C.; Liu, H.; Meng, X.R. Fractional-order modeling and analysis of a three-phase voltage source PWM rectifier. *IEEE Access* **2020**, *8*, 13507–13515. [[CrossRef](#)]
25. El-Khazali, R. Fractional-order LC^αL filter-based grid connected PV systems. In *2019 IEEE 62nd International Midwest Symposium On Circuits And Systems (MWSCAS)*; IEEE: New York, NY, USA, 2019; pp. 533–536.
26. Seo, S.W.; Choi, H.H. Digital implementation of fractional order PID-type controller for boost DC–DC converter. *IEEE Access* **2019**, *7*, 142652–142662. [[CrossRef](#)]
27. Soriano-Sánchez, A.G.; Rodríguez-Licea, M.A.; Pérez-Pinal, F.J.; Vázquez-López, J.A. Fractional-order approximation and synthesis of a PID controller for a Buck converter. *Energies* **2020**, *13*, 629. [[CrossRef](#)]
28. Xie, L.L.; Liu, Z.P.; Ning, K.Z.; Qin, R. Fractional-order adaptive sliding mode control for fractional-order Buck-boost converters. *J. Electr. Eng. Technol.* **2022**, *17*, 1693–1704. [[CrossRef](#)]
29. Azghandi, M.A.; Barakati, S.M.; Yazdani, A. Impedance-based stability analysis and design of a fractional-order active damper for grid-connected current-source inverters. *IEEE Trans. Sustain. Energy* **2021**, *12*, 599–611. [[CrossRef](#)]
30. Wang, Q.Y.; Ju, B.L.; Zhang, Y.Q.; Zhou, D.; Wang, N.; Wu, G.P. Design and implementation of an LCL grid-connected inverter based on capacitive current fractional proportional–integral feedback strategy. *IET Control Theory Appl.* **2020**, *14*, 2889–2898. [[CrossRef](#)]
31. Wang, X.G.; Cai, J.H. Grid-connected inverter based on a resonance-free fractional-order LCL filter. *Fractal Fract.* **2022**, *6*, 374. [[CrossRef](#)]

Disclaimer/Publisher’s Note: The statements, opinions and data contained in all publications are solely those of the individual author(s) and contributor(s) and not of MDPI and/or the editor(s). MDPI and/or the editor(s) disclaim responsibility for any injury to people or property resulting from any ideas, methods, instructions or products referred to in the content.